NeuroImage 47 (2009) 8–17

Contents lists available at ScienceDirect

NeuroImage

journal homepage: www.elsevier.com/locate/ynimg

Predicting the location of entorhinal cortex from MRI

Bruce Fischl [a,b,*], Allison A. Stevens [a], Niranjini Rajendran [e], B.T. Thomas Yeo [b], Douglas N. Greve [a], Koen Van Leemput [a,b], Jonathan R. Polimeni [a], Sita Kakunoori [a], Randy L. Buckner [a], Jennifer Pacheco [f], David H. Salat [a], Jennifer Melcher [d], Matthew P. Frosch [c], Bradley T. Hyman [c], P. Ellen Grant [a], Bruce R. Rosen [a], André J.W. van der Kouwe [a], Graham C. Wiggins [g], Lawrence L. Wald [a], Jean C. Augustinack [a]

[a] *Athinoula A Martinos Center, Department of Radiology, MGH, Harvard Medical School, USA*
[b] *MIT Computer Science and AI Lab, USA*
[c] *Department of Neurology, MGH, Harvard Medical School, USA*
[d] *Department of Otology and Laryngology, MGH, Harvard Medical School, USA*
[e] *RUSH Alzheimer's Disease Center, RUSH University Medical Center, 600 S. Paulina, Suite 1044, Chicago, IL 60612, USA*
[f] *Department of Psychology, The University of Texas at Austin, USA*
[g] *Center for Biomedical Imaging, NYU Medical Center, New York, NY, USA*

ARTICLE INFO

Article history:
Received 23 January 2009
Revised 23 March 2009
Accepted 7 April 2009
Available online 16 April 2009

Keywords:
Morphometry
MRI
Alzheimer's disease

ABSTRACT

Entorhinal cortex (EC) is a medial temporal lobe area critical to memory formation and spatial navigation that is among the earliest parts of the brain affected by Alzheimer's disease (AD). Accurate localization of EC would thus greatly facilitate early detection and diagnosis of AD. In this study, we used ultra-high resolution *ex vivo* MRI to directly visualize the architectonic features that define EC rostrocaudally and mediolaterally, then applied surface-based registration techniques to quantify the variability of EC with respect to cortical geometry, and made predictions of its location on *in vivo* scans. The results indicate that EC can be localized quite accurately based on cortical folding patterns, within 3 mm *in vivo*, a significant step forward in our ability to detect the earliest effects of AD when clinical intervention is most likely to be effective.

Introduction

In the medial temporal lobe, the hippocampal formation and in particular the entorhinal cortex (EC) – the anterior parahippocampal gyrus – show the most significant neurofibrillary tangle pathology and neuronal death early in Alzheimer's disease (Gomez-Isla et al., 1996a, b) and it is the most profoundly affected in the later stages of disease (Arnold et al., 1991a,b; Braak and Braak, 1991). It is widely accepted that neurofibrillary tangle pathology originates in specific layers of the multimodal areas, entorhinal and perirhinal cortex (Braak and Braak, 1985; Van Hoesen and Solodkin, 1993). The EC receives direct projections from frontal, occipital, parietal and other regions of temporal cortex, and provides the major convergent input from these areas to the hippocampus, serving as a gateway for neocortical information, in part for memory processing. Profound degeneration of EC layer II, the entorhinal output layer to the hippocampus through the perforant pathway, is found early in the disease and results in an isolation of the hippocampus from the neocortex (Hyman et al., 1984). Alzheimer's disease is the most common form of dementia and affects over four million people in the United States alone (Albert, 1996), highlighting the importance of being able to localize this cortical area *in vivo*.

Although definitive diagnosis of AD still rests on laborious pathological assessment, volumetric *in vivo* MRI has made notable contributions to reveal atrophy in mesocortical and allocortical areas early in the course of the disease, and has been shown to discriminate controls from AD (De Toledo-Morrell et al., 2000; Dickerson et al., 2001; Insausti et al., 1998; Killiany et al., 2000). Furthermore, *in vivo* volumetric studies have also shown that EC is atrophic in mild cognitive impairment patients, that decreased volume of the hippocampus can predict mild AD (Pennanen et al., 2004) and that clinical progression is correlated with gray matter volume reduction (Jack et al., 2000; Kaye et al., 1997). Nevertheless, it is not possible to observe and detect neuronal level resolutions *in vivo*.

Standard *in vivo* anatomical brain imaging protocols produce images that cannot resolve structures smaller than 1–2 mm in size. Achieving significantly higher resolution would be of fundamental clinical and neuroscientific value, as it would allow the *in vivo* detection and analysis of cytoarchitectural features of the cortex, as well as substructures of brain regions such as the hippocampus, thalamus and amygdala. Unfortunately, such resolution is extremely difficult to obtain *in vivo*, as the signal-to-noise ratio (SNR) goes down with the third power of the linear dimension of each voxel. While

---

* Corresponding author. Athinoula A Martinos Center, Massachusetts Gen. Hosp/ Harvard Medical School, Bldg. 149, 13th St., Charlestown, MA 02129, USA. Fax: +1 617 726 7422.

E-mail address: fischl@nmr.mgh.harvard.edu (B. Fischl).

1053-8119/$ – see front matter © 2009 Elsevier Inc. All rights reserved.
doi:10.1016/j.neuroimage.2009.04.033

some recent studies have pushed this limit to under 1–2 mm, this is at the cost of extremely long scan sessions and specialized imaging hardware (Duyn et al., 2007), and even this is still a coarse resolution relative to what is required to visualize correlates of the cytoarchitecture with MRI. With the exception of the line of Gennari, which is one of the few histological features of the cortex that has been detected *in vivo*, at least for part of its extent (Barbier et al., 2002; Clare and Bridge, 2005; Clark et al., 1992), current *in vivo* methods cannot consistently resolve cytoarchitectural features of the cerebral cortex.

In contrast, ultra-high resolution *ex vivo* MRI can distinguish cytoarchitectural features. In a previous study, using *ex vivo* MRI and a 7 Tesla (7 T) scanner, we robustly distinguished the cell-dense layer II islands throughout the extent of EC (Augustinack et al., 2005), and the line of Gennari, a highly myelinated stripe in layer IV in primary visual cortex (Hinds et al., 2008), allowing us to delineate areas based on its microstructural properties. Moreover, EC recently has been mapped using quantitative architectonic techniques (Amunts et al., 2005) showing it to be less variable in volumetric coordinate than many previously mapped neocortical regions. In related work, we have recently shown that cortical folding patterns are excellent predictors for a wide array of histologically-defined architectonic regions (Fischl et al., 2008). In this study we found that the boundaries of primary and secondary sensory cortices could be localized to within 2–4 mm based on cortical folding patterns, although higher cortical areas such as BA 44/45 were more variable with respect to cortical geometry. The ability to detect cytoarchitecture with *ex vivo* MRI makes these images ideal for the construction of models for the location of cytoarchitectonically defined boundaries that can ultimately to be applied to *in vivo* data sets.

The current way that neuroimaging researchers localize a Brodmann area is problematic and the existing imaging localization methods have limited accuracy. Originally, Brodmann areas were described histologically by Korbinian Brodmann almost a century ago who defined these areas using a Nissl stain and categorized them based on the presence, absence or a combination of cortical layers in a particular region (Brodmann, 1909). Currently there are two common methods that neuroimagers use to localize a Brodmann area. First, neuroimaging researchers identify Brodmann areas based on an *ad hoc* assessment of the location of interest relative to surrounding folding patterns. This approach is problematic as there is no means to rigorously test the uncertainty of these localizations and the relationship between the Brodmann areas (BAs) and cortical folds is sometimes unclear. An alternative is to use volumetric registration to an atlas coordinate system (i.e. the Talairach coordinate system (Talairach et al., 1967; Talairach and Tournoux, 1988)), then map the BAs defined in the atlas onto individual subjects using the registration. Unfortunately, this technique has been shown to yield poor localization accuracy in a wide array of cortical areas (Amunts et al., 2000; Amunts et al., 1999; Geyer et al., 1997; Geyer et al., 2000; Malikovic et al., 2007; Rademacher et al., 2002; Rademacher et al., 2001). Thus, accurate *in vivo* identification and localization of cortical areas – specifically the EC – would be a significant step towards detecting AD pathology in the earliest stages and provide a critical MRI diagnostic tool.

Here we take a novel approach to identification and area localization, and image *ex vivo* tissue samples, in which exceedingly high resolution is obtainable, on the order of 100 μm isotropic, then apply the information derived from the *ex vivo* images to model the probabilistic relationship between cortical geometry and the underlying cytoarchitecture, allowing us to accurately predict the locations of cortical areas from standard *in vivo* imaging data. In the current study we extend beyond sulcal topography and use MR-cytoarchitecture to detect and focus on the localization of EC since it is known to be one of the earliest loci of Alzheimer's disease (AD), and critical for normal memory function. We show that surface-based registration aligns the borders of EC extremely well across subjects, within 2–3 mm, or less than the size of an average functional MRI voxel. The ability to more accurately localize this cortical region is a critical step in the early diagnosis of AD, and in the assessment of the efficacy of potential clinical interventions.

Methods

Participants and ex vivo samples

The *in vivo* AD participants ($n=61$) had a mean and standard deviation of 77.7 ± 6.8 years of age with a range of 63–92 years old. Thirty-one women and thirty men participated. The Clinical Dementia Rating (CDR) was 0.5 for all and the Mini-Mental State Examination (MMSE) was 25.6 ± 3.3. The normal control participants ($n=73$) had a mean age of 76.8 ± 6.9 years with a range of 63–95 years. Forty-seven women and twenty-six men were imaged. The control subjects were CDR = 0 and the MMSE for the control subjects was 28.5 ± 3.7.

The autopsy samples ($n=17$) used in the high resolution *ex vivo* scanning had a mean age of 66.6 ± 12.68 years with a range of 42–81. The gender classification for the *ex vivo* brain samples was ten males (5/5 left/right hemisphere) and two females (1/1 left/right hemisphere), while the remainder of gender information was unavailable. The postmortem interval had a range of 6.5 h to 25 h. Postmortem interval was always limited to less than 25 h in this study. To the best of our knowledge, the *ex vivo* samples did not have any neurological conditions and were presumably cognitively normal.

Description of coils

The images used in this study were acquired using one of three custom-built coils, varying in size to accommodate variations in tissue sample size. That is, we imaged each sample in the smallest coil that would (a) fit the entire sample, and (b) yield high sensitivity over the predicted region containing EC. Specifically, we used either a 4-turn solenoid coil (28.5 mm inner diameter, 44 mm length), a 4-channel phased-array (a linear array of loop coil elements each with 5 cm coil diameter, 1.5 cm overlap between adjacent elements, 16 cm in length) or a small birdcage (24 rungs, outer diameter = 19.7 cm, inner diameter = 19.3 cm, length = 12 cm) for imaging hemispheres without introducing cuts into the tissue samples.

Optimizing ex vivo MR acquisition

In order to compute acquisition parameters that are optimal for revealing the EC architectonics, we utilized a set of techniques for using multi-echo FLASH (MEF) scans acquired at varying flip angles and/or repetition times (TR) to estimate the underlying tissue parameters that are the source of image contrast in standard gradient echo sequences (i.e. T1, proton density (PD) and T2*) (Fischl et al., 2004). Once these parameters were estimated, they were used as input to simulations designed to maximize the contrast-to-noise ratio (CNR) per unit time. We applied these techniques to a set of fixed *ex vivo* tissue samples, imaged with abovementioned radio frequency coils on a 7 T human scanner (Siemens Medical Systems, Erlangen, Germany). The data was acquired using a MEF sequence, with $TR=40$ ms, $\alpha=15°,20°,25°$, 4 echoes, $TE=8$ ms, 16 ms, 24 ms, 32 ms) at 100 μm isotropic resolution. The multiple flip angles were used to estimate the T1 and proton density of the underlying formalin-fixed tissue using the techniques described in (Fischl et al., 2004). In addition, the multiple echoes were used to estimate T2* using a log-linear fit to the data. Region of interests (ROIs) were then manually drawn in the gray and white matter, and the mean tissue parameters were computed to be: $T1=(WM=770$ ms, $GM=1078$ ms), $PD=(WM=18{,}024$ ms, $GM=19{,}996$ ms), and $T2^*=(WM=11$ ms, $GM=26$ ms). An example of the data (first four images) and the

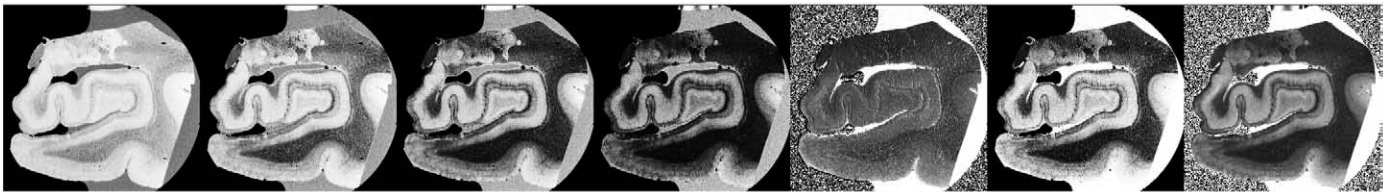

Fig. 1. Multi echo flash (images 1–4) with fitted T1 (image 5), PD (image 6) and T2* (rightmost image).

parameter maps (last three images) is given in Fig. 1. Interestingly, the dominant source of image contrast in these fixed *ex vivo* samples is given by T2* differences in the tissue.

Using these parameters, the steady state Bloch equations were applied (Bloch et al., 1946) and the CNR was computed over TR = [5 ms,80 ms], TE = [5 ms, TR-2 ms], and flip angle $\alpha = [3°,40°]$. For each TR/TE/α pair, the CNR was computed by assuming a symmetric readout, a minimum bandwidth and assuming that 2 ms are required for spoiling at the end of each TR. The CNR was assumed to increase with the 1/2 power of the number of echoes that can be acquired for a given TR and echo spacing, and to decrease with the square root of TR, corresponding to the assumption that the noise is time-independent (that is, a longer TR implies that fewer scans can be collected and averaged to increase SNR). The optimum acquisition parameters from this simulation were computed to be TR = 40 ms, TE = 20 ms, and $\alpha = 23°$. These parameters allowed us to acquire images that permitted the direct visualization of the layer II entorhinal islands as shown in Figs. 2 and 3. The presence of these islands allowed one of us (JCA) to manually delineate the borders of EC on the high resolution samples. These borders were then transferred back to a set of 1 mm isotropic acquisitions (1.5 T, MEF,TR = 20 ms, $\alpha = 5°, 10°, 15°, 20°, 25°, 30°$, 8 echoes, TE = 1.85 ms to 15.85 ms, with a 2 ms echo spacing) which were used to generate surface models of the cortex (Dale et al., 1999; Fischl et al., 2001; Fischl et al., 1999a,b). More specifically, the high resolution 7 T data was manually registered to the 1.5 T data, and this registration was used to map the EC label into the low resolution coordinate system. The labels were then sampled onto the gray/white surface boundary model, and small sampling artifacts were corrected using a third-order binary close (3 binary dilations, followed by 3 binary erosions, to remove small holes in the label, due to differential distortion in the 7 T and 1.5 T images). An example of these surfaces together with the EC labels sampled onto inflated surface models is given in Fig. 4.

Basic anatomy and connectivity of the MTL

The medial surface of the temporal lobe contains a number of structures that are critical for memory, emotion, and olfactory neural processes. Most broadly, this region includes primary olfactory cortex, the amygdala, and the hippocampal formation and overlying parahippocampal gyrus. The hippocampal formation can be subdivided into the hippocampus proper (or cornu ammonis), the dentate gyrus, and the subiculum. The majority of extrinsic afferents to the hippocampus arise from entorhinal (area 28 and 34), perirhinal (area 35) and posterior parahippocampal cortices (areas TH and TF in the monkey). Supragranular entorhinal fibers project to the molecular layer in dentate gyrus through a white matter tract known as the *perforant pathway*, and the dentate gyrus in turn projects to the CA3 subfield of the hippocampus via the mossy fiber pathway. The CA3 subfield projects intrinsically via Schaffer collaterals to the fimbria-fornix and to pyramidal cells in CA1 subfield, which in turn projects back to deep pyramidal neurons in EC. But the majority of efferent fibers from the hippocampus take a less direct route that first terminates in the subiculum (ammonic-subicular pathway) and then travels out of the formation through the fornix and EC (Rosene and Van Hoesen, 1987).

Anatomically, EC makes up the anterior portion of the parahippocampal gyrus and we utilized three distinctive cytoarchitectural characteristics to define it: *(i)* the cell-dense layer II islands, *(ii)* the cell poor lamina dissecans (ld) and *(iii)* deep pyramidal layer. Layer II is arranged in clusters or islands that are neuron dense regions alternating with neuron poor regions. The lamina dissecans is an acellular layer that is unique to the EC and the deep pyramidal layer in EC is homogenous and fairly wide to receive subicular input.

Description of validation and labeling in EC

To show validation of our methods, Fig. 2 illustrates the corresponding high resolution (100 µm) MRI (Fig. 2A) and the Nissl stained section (Fig. 2B). The mediolateral boundaries of entorhinal layer II islands are outlined with white arrows in MRI and black arrows in Nissl section (Figs. 2A and B, respectively). In both image modalities, MRI and Nissl, the medial border is inferior to the parasubiculum and the medial most entorhinal island in lamina II is highlighted with a white arrow. The alternations in signal in layer II EC marking the islands as well as the low signal intensities in the lamina

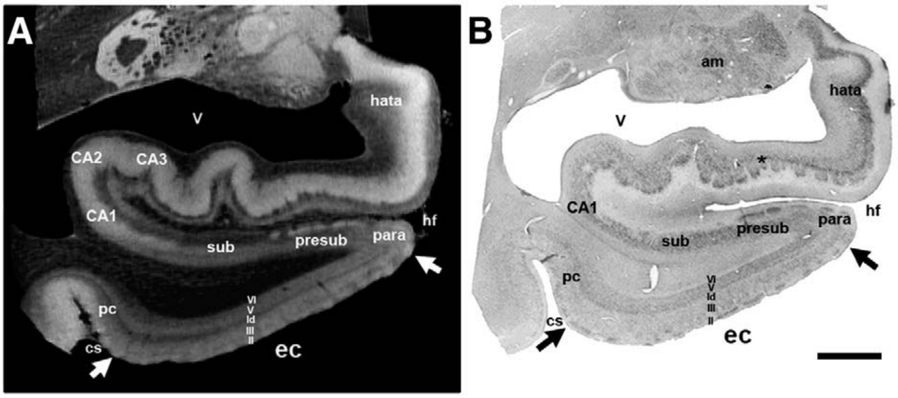

Fig. 2. The matching high resolution (100 µm) MRI in (A) and the Nissl stained section in (B). Image and photomicrograph are presented to illustrate and validate our *ex vivo*-histology methods. Magnification bar = 1 cm. am = amygdala; CA1–CA3 = ammon's horn fields; cs = collateral sulcus; ec = entorhinal cortex; hata = hippocampal-amygdala-transition-area; hf = hippocampal fissure; sub = subiculum; para = parasubiculum; pre = presubiculum; pc = perirhinal cortex; v = ventricle.

dissecans can be observed in high resolution MRI as shown in Fig. 2, which compares the high resolution MRI (A) with a Nissl stain (B), illustrating that both reveal the laminar architecture of the EC. The lamina II, III, lamina dissecans (ld), V and VI are outlined (Fig. 2), following Cajal's nomenclature for the cell free lamina in layer IV (i.e. lamina dissecans). The lateral border of entorhinal lies at the lateral apex of the parahippocampal gyrus and typically coincides with the opening of the collateral sulcus, albeit the sulcal patterns in medial temporal lobe can be quite variable. The borders of EC were manually delineated using these features by a trained neuroanatomist (JCA) on a set of 9 left hemisphere and 8 right hemisphere samples, taken from neurologically normal subjects. An additional example of the robustness of these features, and in particular the layer II entorhinal islands is given in Figs. 2 and 3.

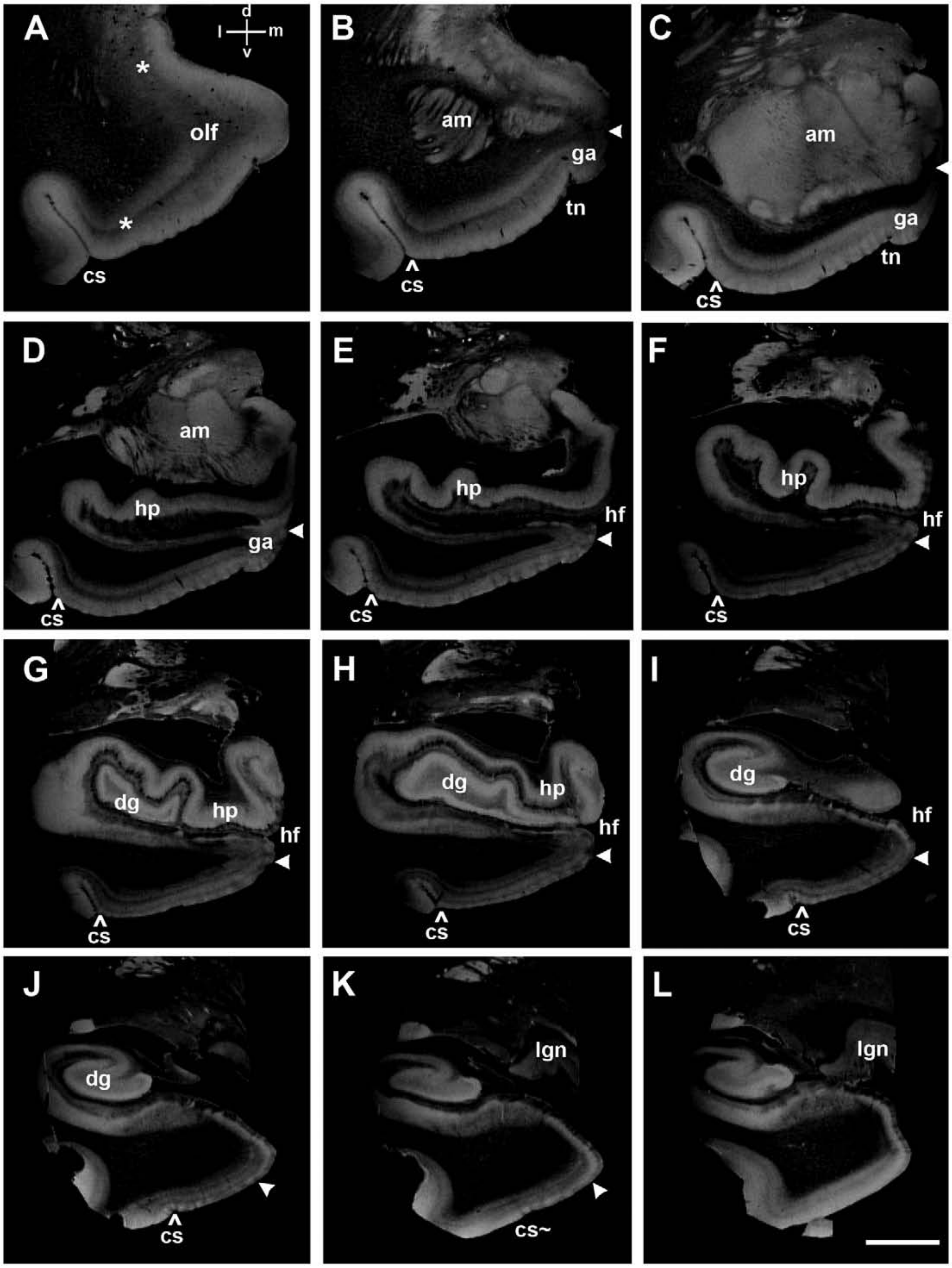

Fig. 3. The rostrocaudal and mediolateral limits of EC in high resolution *ex vivo* MRI (100 μm isotropic voxels). (A) Primary olfactory cortex is loosely marked with asterisks and anterior EC is between the lateral asterisk and 'olf' label. A coordinate system is labeled, 'd' for dorsal, 'v' for ventral, 'l' for lateral and 'm' for medial in A for all panels. White arrowheads throughout this figure demarcate the medial entorhinal boundary while the caret (^) demarcates the lateral entorhinal limit. (B–D) show EC at the level of gyrus ambiens (area 34) with the tentorial notch distinguishing entorhinal area 34 from entorhinal area 28. (E–H) demonstrate the 'pes' hippocampi at the uncal hippocampal level. (I) shows the ending of the hippocampal head and the size of the parahippocampal gyrus is becoming smaller. (J) and (K) display the posterior EC and concurrently the collateral sulcus ends (cs~) in (K) at approximately the level of the lateral geniculate nucleus. At level (L), entorhinal islands are no longer observed. Abbreviations: am = amygdala; cs = collateral sulcus; ec = entorhinal cortex; dg = dentate gyrus; ga = gyrus ambiens; hp = hippocampus; hf = hippocampal fissure; olf = olfactory; lgn = lateral geniculate nucleus; sub = subiculum; para = parasubiculum; pre = presubiculum; pc = perirhinal cortex; tn = tentorial notch. Magnification bar = 1 cm.

Results

Delineation of the borders of EC

We analyzed all rostrocaudal levels of the EC with special attention to the rostral, caudal, medial and lateral borders of the EC. In Fig. 3, the rostrocaudal extent of EC is illustrated showing the rostral most and caudal most boundaries in A and K, respectively. At the rostral end, primary olfactory cortex occupies the anterior most portion of EC (Fig. 3A) and some reports have described this cortex as subregion EO (Insausti et al., 1995) or prorhinal (Krimer et al., 1997). Although primary olfactory cortex exhibits a slight clustering in its superficial layers, it does not contain large stellate neurons that are prototypical of the mid and posterior levels of EC. It is difficult to discern layer II in *ex vivo* MRI in primary olfactory cortex because the lamina are thinner and not organized into discrete clusters (Fig. 3A). The classic layer II islands are beginning to organize at this anterior plane and a hint of clustering can be observed immediately to the right of the lateral asterisk (Fig. 3A). The medial border changes the most throughout this cortex because of the presence of the gyrus ambiens (area 34) anteriorly. At anterior levels, the medial border abuts the amygdala nuclei (Figs. 3B–D). Moving caudally along the parahippocampal gyrus, the gyrus ambiens disappears and gives way to the hippocampal fissure (Fig. 3E). Once the hippocampal fissure opens, the EC borders the parasubiculum medially (Figs. 3E–K). We have delineated the medial border with a white arrowhead in relevant panels in Fig. 3. Laterally, the EC borders perirhinal cortex (Brodmann's area 35) and this lateral border is routinely observed at the lateral crown or apex of the parahippocampal gyrus (Figs. 3A–K). Some reports have referred to this lateral apex as the shoulder of the parahippocampal gyrus (De Toledo-Morrell et al., 2000). EC's lateral border is demarcated with a caret (^) in Fig. 3 directly above the 'cs' which stands for collateral sulcus. Perirhinal cortex lies on the medial bank of the collateral sulcus and is immediately lateral to EC. As the collateral sulcus ends posteriorly (cs~ in Fig. 3K), the posterior EC is winding down as well; it is observed in our *ex vivo* MR images for few additional slices (i.e. Fig. 3K) and is completely gone at the next illustrated level (Fig. 3L). The caudal limit of the EC is at the level of the lateral geniculate nucleus of the thalamus, approximately half way through the parahippocampal gyrus. In Fig. 3L, the entorhinal islands in layer II are no longer observed because the EC ends here. Taken together, the panels in Fig. 3 illustrate EC in its entirety and shows the comprehensive – anterior, posterior, medial and lateral – borders of EC, Brodmann's area 28 and 34 in *ex vivo* MRI.

Validation of labeling using surface models

We imaged 17 human hemispheres at 1.5 T at 1 mm *ex vivo* in order to construct surface models for the same subjects for which we delineated the borders of EC using the *ex vivo* 100 µm isotropic data based on its architectonic properties (shown in Fig. 3). The high resolution *ex vivo* scans were manually registered to the 1 mm *ex vivo* scans using a rigid transformation in order to transfer the labels drawn on the 100 µm data to the surface models. The set of labels delineated on the 100 µm data transformed to the 1.5 T data used for surface reconstructions are shown in a medial view of each *ex vivo* subject's inflated surface in Fig. 4 (left and right hemispheres).

In order to quantify the variability of the predicted location of EC across subjects we used a modified symmetric Hausdorff distance. Specifically, for each point on the boundary of each subject's EC label in the individual subject space, we computed the minimum distance to the boundary of each other subject projected into the individual subject's surface model, then computed the average of these. The results of this analysis are displayed in Fig. 5. The advantage of this

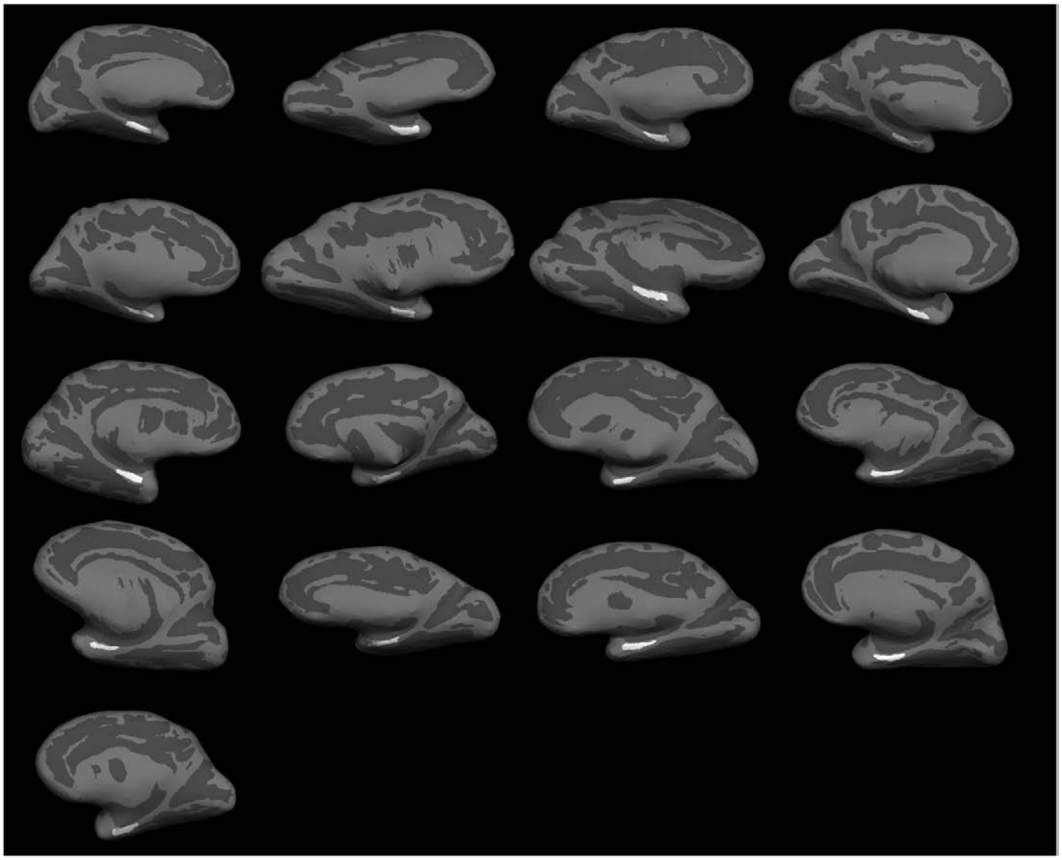

Fig. 4. Medial view of the entorhinal labels used in this study. *Ex vivo* EC labeling shown on inflated surface of the brain.

procedure is that it provides a measure in millimeters of the uncertainty of localization. In addition, it is not biased by the size of an area, a well-known problem for other similarity measures such as the Dice or Jaccard coefficients (Jaccard, 1912), which compute the degree of overlap of binary labels, which is affected by the size of the label, with larger labels typically evidencing greater overlap than smaller one.

In order to visualize the spatial variability, we mapped each label into a common spherical coordinate system and built cross-subject spatial probability maps that each point on the surface is part of EC, as shown in Fig. 6. Each point in each hemisphere in this figure is color-coded to reflect the probability that that point in the average spherical coordinate system is part of EC. Thus a perfectly predicted EC would be reflected by a step function transitioning from 100% overlap (all subjects) in the interior of EC (yellow), to 0% overlap (no subjects) outside of EC (gray). These data illustrate the medial temporal localization of EC in the anterior parahippocampal gyrus in both left and right hemispheres.

To illustrate the clinical utility of the accurate localization of EC, we used spherical registration (Fischl et al., 1999a,b) to predict the location of EC in a set of subjects diagnosed with very mild Alzheimer's disease (AD, $N = 61$, CDR = 0.5, men/women = 30/31, age = 77.7 ± 6.8 (63–92)) as well as healthy controls ($N = 73$, men/women = 26/47, age = 76.8 ± 6.9 (63–95)). We then used our surface-based tools to reconstruct models of the gray/white and pial surfaces (Dale, 1994; Dale et al., 1999; Fischl et al., 2001; Fischl et al., 2004; Fischl et al., 2002a,b; Fischl et al., 1999a,b) and to measure the mean thickness of the cortex in the predicted EC (Fischl and Dale, 2000). The results of this analysis are shown in Fig. 7, showing that even in this early stage of clinical AD we are able to detect robust thickness differences ($p < 10^{-5}$) in the predicted location of EC, in agreement with previous studies that either showed EC effects in cortical maps or used manual techniques to localize EC (De Toledo-Morrell et al., 2000; Detoledo-Morrell et al., 1997; Dickerson et al., 2001; Dickerson et al., 2004; Dickerson et al., 2008; Du et al., 2001; Gomez-Isla et al., 1996a,b; Killiany et al., 2000; Killiany et al., 2002; Xu et al., 2000). As a control for this result we also drew two additional ROIS. The first ROI represented the entire temporal lobe, excluding the estimated location of EC. The second was drawn beginning one centimeter posterior to the predicted location of EC, extending posteriorly the same length as the predicted EC. We then performed the same analysis of cortical thickness across the two populations within these ROIs. The results of this analysis are given in Fig. 7. The greatly reduced cortical thickness in EC (Fig. 7, left) relative to both the posterior medial temporal lobe (Fig. 7, center) and the entire non-EC temporal lobe (Fig. 7, right), illustrate that our results are in fact specific to EC and not representative of widespread cortical thinning.

As shown above, the surface geometry predicted the location of right EC more accurately than left EC. In order to assess whether geometric variations in the folding patterns contributed to the variability in localization accuracy in the current dataset we examined the sulcal pattern in the medial temporal lobe and specifically the collateral sulcus, one of the primary landmarks used for *in vivo* estimation of EC borders (Insausti et al., 1998). Visual inspection revealed that four of the nine left hemisphere samples had a single uninterrupted collateral sulcus and the remaining five cases showed an interrupted and/or branching collateral sulcus. For the right hemispheres, three cases displayed a single uninterrupted collateral sulcus, while five cases showed an interrupted or branched pattern. Since these patterns were somewhat evenly split between uninterrupted and interrupted configurations and because of the small sample size, it is difficult to interpret whether the sulcal outline had an effect. The case with the largest error exhibited a single uncomplicated collateral sulcus, suggesting that the variability of the collateral sulcus by itself may not be the determining factor in localization accuracy.

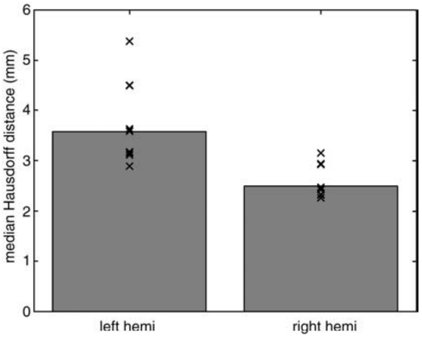

Fig. 5. Symmetric mean Hausdorff distances for the left hemisphere (left) and right hemisphere (right). The bars plot the median of the individual points.

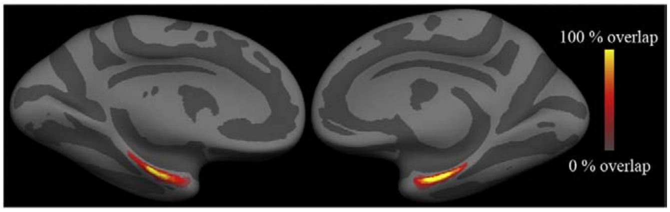

Fig. 6. Spatial probability maps for EC in the left and right hemispheres.

Discussion

Sulcal patterns in the medial temporal lobe are notoriously variable in the human brain (Insausti, 1993; Insausti et al., 1998; Novak et al., 2002; Ono et al., 1990; Van Hoesen et al., 2000), making manual parcellation of these critical areas based on visual inspection of cortical geometry extremely difficult. The architectonic properties of EC however are much more well-characterized (e.g. (Amunts et al., 2005; Augustinack et al., 2004; Cajal, 1909; de No, 1933; Insausti et al., 1995; Krimer et al., 1997; Solodkin and Van Hoesen, 1996)). Using ultra-high-field (7 T) and ultra-high resolution (≈100 µm isotropic) *ex vivo* MRI we were able to directly visualize the architectonic features that distinguish EC from adjacent regions and to use them to manually delineate the borders of EC. These borders were mapped onto whole-hemisphere MRI acquired at lower field (1.5 T), and subsequently onto surface models of the cerebral cortex constructed from the low-field volumes (Dale et al., 1999; Fischl et al., 2001; Fischl et al, 1999a,b). We then applied surface-based inter-subject registration techniques (Fischl et al., 2008; Fischl et al., 1999a,b; Hinds et al., 2008) that align cortical folding patterns to determine how well the cortical folds predicted the location of the microscopically defined borders of EC. As shown in the Results section, the EC borders were in fact localized extremely well by the surrounding geometry, with variability in the location of the borders on the order of 3 mm. Interestingly, the lateralization of these effects qualitatively agrees with Amunts et al. (2005), in that the location of left hemisphere EC was more variable (≈3.5 mm) than the right hemisphere (≈2.5 mm) with respect to the folding patterns, although a larger sample size will be required to confirm this finding. It is also worth pointing out that the accuracy of EC localization is comparable to that of primary sensory areas (Fischl et al., 2008), perhaps due to its connectivity with the hippocampus, which has a relatively stable location with respect to other brain structures.

The EC islands (lamina II) were apparent on the *ex vivo* MRI throughout the rostrocaudal EC in agreement with subdivisions proposed in previous microscopy studies by Insausti et al. (1995) and Krimer et al. (1997). The anterior most regions (i.e. EO of Insausti; PR of Krimer) and medial most regions (i.e. EMI of Insausti; 28Is of

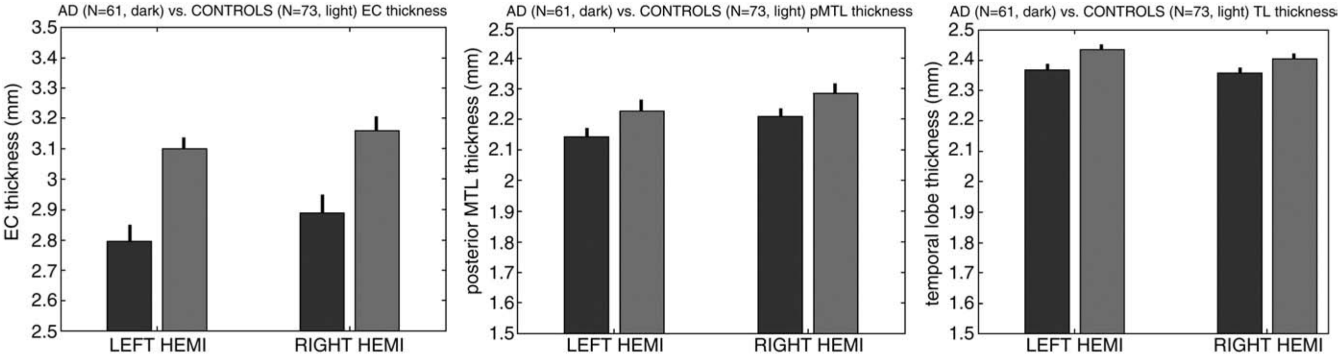

Fig. 7. Comparison of AD and control mean cortical thickness in EC (left), posterior medial temporal lobe (center) and the entire temporal lobe excluding the predicted location of EC (right). The black bars represent the standard error of the mean in a random effects analysis across subjects.

Krimer) have thinner layer II and are more difficult to detect. In our studies we have found that even modest reduction in resolution from 100 μm to 120 μm isotropic voxels can make the EC borders in these regions difficult or impossible to detect. Conversely, the more lateral subregions of EC (i.e. 28Ir and 28Ic of Krimer; EI of Insausti) have thicker, rounded and sometimes even elongated layer II islands compared to medial and anterior regions (Insausti et al., 1995; Krimer et al., 1997), and are more readily apparent at coarser resolutions.

The entorhinal lamina nomenclature also deserves some discussion. While Cajal identified the cell free layer as layer IV (i.e. lamina dissecans), his student, Lorente de Nó, referred to the lamina dissecans as layer IIIa and layer IV to the large pyramidal neurons deep to the lamina dissecans (Cajal, 1909; de No, 1933). In this report, we have followed the nomenclature of Cajal, which agrees with the definition of periallocortex that lacks a granular layer. However, it is important to note that the deep pyramidal neurons in EC are in a unique position because they receive such a strong projection from the subiculum. The deep pyramidal neurons could be thought of as a continuation of the subiculum, even illustrated as such in Lorente de Nó's 1934 paper, which is why Lorente de Nó's nomenclature is attractive; it makes sense given the hippocampal/EC connections. Although the neurogenesis of EC is poorly understood, Filimonoff (1947) had suggested that the superficial layers of EC were derived from paleocortex (olfactory) cortex and the deeper layers originated from allocortex (hippocampal) cortex. Filimonoff's notion was that two three-layered cortices came together to form a rudimentary six layered cortex, EC. Even though this topic is beyond the scope of this manuscript, Filimonoff's reasoning may be an explanation for why EC is agranular, its agranularity being represented as lamina dissecans and yet entorhinal contains a deep layer with large pyramidal neurons, a presumptive layer IV. In fact, in the Nissl stained section in Fig. 2, to the right of the lamina labels (i.e. medial EC), one can observe the acellular layer (lamina dissecans), the deep pyramidal layer (presumptive layer IV) and closely opposed layers V and VI.

Although we attempted to match the planes from the MRI and the sectioning tissue, it is nearly impossible to achieve. The hippocampal fissure and medial hippocampal fields illustrate this point markedly in Figs. 2A and B. It is noteworthy that, in this example (Fig. 2), the hippocampal fissure is opened up more in the MRI whereas the Nissl photomicrograph image contains a shorter hippocampal fissure. Furthermore, the medial hippocampus is more posterior in the MRI where it is still transitioning from subicular cortices to CA subfields in the Nissl stained section (noted by * in Fig. 2). One might reason that it is a matter of scrolling anterior in the MR images to find the precise plane, but the planes are oblique by one or two degrees. Until better stereotaxic methods come about for *ex vivo* imaging, these slight differences in planes are unavoidable.

It is interesting to note that previous studies have reported lateralization effects in the medial temporal lobe, in broad agreement with our finding of greater localization accuracy in the right hemisphere EC than in the left. For example, in Ono's categorization of the collateral sulcus in 25 brains (Ono et al., 1990), the left posterior collateral sulcus had the most complicated sulcal topography, while the right was deemed to be less complex with fewer interruptions and connections. In a separate study using *in vivo* subjects, we identified and categorized the collateral sulcus in normal controls and AD cases and found that approximately 20–30% (depending on age) of the normal controls displayed an interrupted collateral sulcus, whereas the incidence was much higher for the AD cases (≈57%) (Feczko et al., 2009). In addition, histologically it has been shown that neuron counts are higher in the left EC than in the right (Simic et al., 2005). Finally, an *in vivo* volumetric imaging study has shown that right EC is a better predictor of early AD than the left EC or either hippocampal region (De Toledo-Morrell et al., 2000), possibly indicative of the greater difficulty of accurately localizing the left EC than the right. Additional studies examining morphometric changes and their correlation with respect to sulcal patterns in large populations are required to further elucidate this relationship.

The ability to accurately predict the location of EC has significance on a number of levels. From a neuroscientific perspective, EC has intriguing structural and functional properties that make it the target of a wide array of animal and human research. Structurally, EC has a unique cortical architecture with layer II neurons organized into alternating clusters of neuron dense “entorhinal islands” and neuron poor inter-island regions (de No, 1933; Ramon y Cajal, 1909). Functionally, entorhinal efferent axons project to the hippocampal formation via the perforant pathway through which most afferent neocortical information converges and is destined for hippocampal circuitry. The EC (layer IV) also receives the hippocampal CA1-subicular projection and layer IV ultimately projects back to the neocortex (Van Hoesen and Pandya, 1975a,b) so EC sits at a critical juncture anatomically and connectionally in the human brain.

The EC has been shown to contain topographic maps of the visual environment with layer II “grid cells” that appear to encode spatial maps of the environment (Hafting et al., 2005), with lateral entorhinal showing less spatial selectivity than medial entorhinal (Hargreaves et al., 2005). The spatial maps are arrayed in an intriguing hexagonal arrangement of “grid cells”, with variable spacing as one moves from dorso-lateral EC to ventro-medial EC (Fyhn et al., 2004). In addition, EC has been shown to myelinate in adolescence, and there is evidence that it is affected in schizophrenia (Arnold et al., 1991a,b; Arnold et al., 1997; Benes, 1989, 1993; Benes et al., 1994; Harrison, 1999; Kalus et al., 2005; Prasad et al., 2004; Talamini et al., 2005; Turetsky et al., 2003). Thus, accurate localization of EC may help future functional studies to further characterize spatial navigation systems, and to detect developmental abnormalities in the brain in addition to changes observed in AD in this region.

Clinical assessment can diagnose probable AD with a high degree of accuracy, yet a confirmed diagnosis of AD can only be made via histological analysis of the postmortem brain. The postmortem diagnosis of AD is based on the regional distribution of characteristic lesions including neuritic amyloid plaques and neurofibrillary tangles in limbic and association cortices (Arnold et al., 1991a,b; Arriagada et al., 1992; Gomez-Isla et al., 1996a,b; Hyman and Gomez-Isla, 1997; Perry et al., 1986; Rogers and Morrison, 1985; Terry and Katzman, 1983). Histological changes in the EC occur early in the disease process (Braak and Braak, 1991; Giannakopoulos et al., 1997; Gomez-Isla et al., 1996a,b). In fact, even non-demented older adults occasionally show the required pathology for an AD diagnosis at autopsy (Katzman et al., 1988). Although still open to debate, a consensus is growing that such 'incidental' changes represent the earliest (preclinical) stages of AD pathology, even in cognitively healthy adults (Berg et al., 1998; Hyman, 1997). Regional plaque and tangle deposition follows a characteristic spatiotemporal distribution in the brain (Arnold et al., 1991a,b; Braak and Braak, 1991, 1997), with early degeneration manifest in the hippocampal formation and temporo-parietal cortex, and later effects found in prefrontal regions.

It is clear that regions showing greatest pathology in postmortem studies are morphologically altered in MRI (Fischl et al., 2002a,b; Fox et al., 2001; Jack et al., 1999; Jack et al., 1997; Kaye et al., 1997; Pearlson et al., 1992). The longitudinal rate of volume loss in these structures is useful for the discrimination of probable AD from normal aging with accuracy that approaches clinical diagnosis (Crum et al., 2001; Fox et al., 2001; Jack et al., 1998; Kaye et al., 1997; Laakso, 2002; Scahill et al., 2002). Neuroimaging techniques can be used to detect volumetric changes in these regions prior to the onset of dementia and even prior to the onset of cognitive decline (Convit et al., 1997; Jack et al., 1999; Kaye et al., 1997; Killiany et al., 2000; Killiany et al., 2002; Xu et al., 2000). Recent studies demonstrate the ability to measure degenerative changes in cortical gray matter *in vivo*, and relate such measures to cognitive ability (e.g., delayed recall) and disease severity (Convit et al., 1997; de Toledo-Morrell et al., 2000; Fischl et al., 2002a,b; Killiany et al., 2002; Laakso et al., 2000; Laakso et al., 1995; Mungas et al., 2001; Petersen et al., 2000; Soininen et al., 1994). MRI measures predict which healthy older adults, or older adults with MCI will subsequently become demented (Fischl et al., 2002a,b; Jack et al., 1999; Kaye et al., 1997).

Clinical intervention in AD would be greatly facilitated by an accurate method of detecting the disease early in its course, before widespread neuronal death has occurred. This is technically difficult, as the early effects are subtle and localized to a small number of brain regions, such as EC. The ability to localize the region of expected change and the accurate quantification of the change are critical tools in MRI. In this report, we have shown that surface-based geometry-driven inter-subject registration tools can resolve the first of these problems by accurately predicting the borders of the EC based on the surrounding surface geometry, which we believe to be an important step towards the development of techniques for the early diagnosis and monitoring of diseases such as AD.

Acknowledgments

Support for this research was provided in part by the National Center for Research Resources (P41-RR14075, and the NCRR BIRN Morphometric Project BIRN002, U24 RR021382), the National Institute for Biomedical Imaging and Bioengineering (R01 EB001550, R01EB006758), the National Institute for Neurological Disorders and Stroke (R01 NS052585-01) as well as the Mental Illness and Neuroscience Discovery (MIND) Institute, and is part of the National Alliance for Medical Image Computing (NAMIC), funded through the NIH Roadmap for Medical Research, Grant U54 EB005149. Additional support was provided by The Autism & Dyslexia Project funded by the Ellison Medical Foundation. Finally, we acknowledge a research agreement and research support from Siemens Healthcare. One of the authors (LLW) has obtained consulting income from Siemens Healthcare.

References

Albert, M.S., 1996. Cognitive and neurobiologic markers of early Alzheimer disease. Proc. Natl. Acad. Sci. 93, 13547–13551.

Amunts, K., Schleicher, A., Bürgel, U., Mohlberg, H., Uylings, H.B.M., Zilles, K., 1999. Broca's region revisited: cytoarchitecture and intersubject variability. J. Comp. Neurol. 412, 319–341.

Amunts, K., Malikovic, A., Mohlberg, H., Schormann, T., Zilles, K., 2000. Brodmann's areas 17 and 18 brought into stereotaxic space — where and how variable? NeuroImage 11, 66–84.

Amunts, K., Kedo, O., Kindler, M., Pieperhoff, P., Schneider, F., Mohlberg, H., Habel, U., Shah, J.N., Zilles, K., 2005. Cytoarchitectonic mapping of the human amygdala, hippocampal region and entorhinal cortex. Anat. Embryol. 210, 343–352.

Arnold, S.E., Hyman, B.T., Flory, J., Damasio, A.R., Van Hoesen, G.W., 1991a. The topographical and neuroanatomical distribution of neurofibrillary tangles and neuritic plaques in the cerebral cortex of patients with Alzheimer's disease. Cereb. Cortex 1, 103–116.

Arnold, S.E., Hyman, B.T., Van Hoesen, G.W., Damasio, A.R., 1991b. Some cytoarchitectural abnormalities of the entorhinal cortex in schizophrenia. Arch. Gen. Psychiatry 48, 625–632.

Arnold, S.E., Ruscheinsky, D.D., Han, L.Y., 1997. Further evidence of abnormal cytoarchitecture of the entorhinal cortex in schizophrenia using spatial point pattern analyses. Biol. Psychiatry 42, 639–647.

Arriagada, P.V., Marzloff, K., Hyman, B.T., 1992. Distribution of Alzheimer-type pathologic changes in nondemented elderly individuals matches the pattern in Alzheimer's disease [see comments] Neurology 42, 1681–1688.

Augustinack, J., Kouwe, A.v.d., Salat, D., Wald, L., Blackwell, M., Wiggins, C., Fischl, B., 2004. Detection of entorhinal islands using 7 T MRI. Human Brain Mapping. Budapest, Hungary.

Augustinack, J.C., van der Kouwe, A.J., Blackwell, M.L., Salat, D.H., Wiggins, C.J., Frosch, M.P., Wiggins, G.C., Potthast, A., Wald, L.L., Fischl, B.R., 2005. Detection of entorhinal layer II using 7Tesla [correction] magnetic resonance imaging. Ann. Neurol. 57, 489–494.

Barbier, E.L., Marrett, S., Danek, A., Vortmeyer, A., Gelderen, P.V., Duyn, J., Bandettini, P., Grafman, J., Koretsky, A.P., 2002. Imaging cortical anatomy by high-resolution MR at 3.0T: detection of the stripe of Gennari in visual area 17. Magn. Reson. Med. 48, 735–738.

Benes, F.M., 1989. Myelination of cortical-hippocampal relays during late adolescence. Schizophr. Bull. 15, 585–593.

Benes, F.M., 1993. The relationship between structural brain imaging and histopathologic findings in schizophrenia research. Harv. Rev. Psychiatry 1, 100–109.

Benes, F.M., Turtle, M., Khan, Y., Farol, P., 1994. Myelination of a key relay zone in the hippocampal formation occurs in the human brain during childhood, adolescence, and adulthood. Arch. Gen. Psychiatry 51, 477–484.

Berg, L., McKeel Jr., D.W., Miller, J.P., Storandt, M., Rubin, E.H., Morris, J.C., Baty, J., Coats, M., Norton, J., Goate, A.M., Price, J.L., Gearing, M., Mirra, S.S., Saunders, A.M., 1998. Clinicopathologic studies in cognitively healthy aging and Alzheimer's disease: relation of histologic markers to dementia severity, age, sex, and apolipoprotein E genotype. Arch. Neurol. 55, 326–335.

Bloch, F., Hansen, W.W., Packard, M., 1946. The nuclear induction experiment. Phys. Rev. 70, 474–485.

Braak, H., Braak, E., 1985. On areas of transition between entorhinal allocortex and temporal isocortex in the human brain. Normal morphology and lamina-specific pathology in Alzheimer's disease. Acta Neuropathol. 68, 325–332.

Braak, H., Braak, E., 1991. Neuropathological staging of Alzheimer-related changes. Acta Neuropathol. (Berl) 82, 239–259.

Braak, H., Braak, E., 1997. Staging of Alzheimer-related cortical destruction. Int. Psychogeriatr. 9, 257–261 discussion 269–272.

Brodmann, K., 1909. Vergleichende Lokalisationslehre der Groβhirnrinde in ihren Prinzipien dargestellt auf Grund des Zellenbaues. Leipzig.

Cajal, S.R., 1909. Histologie du système nerveux de l'homme et des vertébrés. Maloine, Paris.

Clare, S., Bridge, H., 2005. Methodological issues relating to in vivo cortical myelography using MRI. Hum. Brain Mapp. 26, 240–250.

Clark, V.P., Courchesne, E., Grafe, M., 1992. In vivo myeloarchitectonic analysis of human striate and extrastriate cortex using magnetic resonance imaging. Cereb. Cortex 2, 417–424.

Convit, A., De Leon, M.J., Tarshish, C., De Santi, S., Tsui, W., Rusinek, H., George, A., 1997. Specific hippocampal volume reductions in individuals at risk for Alzheimer's disease. Neurobiol. Aging 18, 131–138.

Crum, W., Scahill, R., Fox, N., 2001. Automated hippocampal segmentation by regional fluid registration of serial MRI: validation and application in Alzheimer's disease. Neuroimage 13, 847–855.

Dale, A.M., 1994. Source Localization and Spatial Discriminant Analysis of Event-Related Potentials: Linear Approaches. University of California, San Diego.

Dale, A.M., Fischl, B., Sereno, M.I., 1999. Cortical surface-based analysis I: segmentation and surface reconstruction. NeuroImage 9, 179–194.

de No, L., 1933. Studies on the structure of the cerebral cortex. J. Psychol. Neurol. 45, 381–438.

de Toledo-Morrell, L., Dickerson, B., Sullivan, M.P., Spanovic, C., Wilson, R., Bennett, D.A., 2000. Hemispheric differences in hippocampal volume predict verbal and spatial memory performance in patients with Alzheimer's disease. Hippocampus 10, 136–142.

De Toledo-Morrell, L., Goncharova, I., Dickerson, B., Wilson, R.S., Bennett, D.A., 2000. From healthy aging to early Alzheimer's disease: in vivo detection of entorhinal cortex atrophy. Ann. N.Y. Acad. Sci. 911, 240–253.

Detoledo-Morrell, L., Sullivan, M.P., Morrell, F., Wilson, R.S., Bennett, D.A., Spencer, S., 1997. Alzheimer's disease: in vivo detection of differential vulnerability of brain regions. Neurobiol. Aging 18, 463–468.

Dickerson, B., Goncharova, I., Sullivan, M., Forchetti, C., Wilson, R., Bennett, D., Beckett, L., deToledo-Morrell, L., 2001. MRI-derived entorhinal and hippocampal atrophy in incipient and very mild Alzheimer's disease. Neurobiol. Aging 22, 747–754.

Dickerson, B., Salat, D., Bates, J., Atiya, M., Killiany, R., Greve, D., Dale, A., Stern, C., Blacker, D., Albert, M., Sperling, R., 2004. MRI measures of medial temporal lobe function and structure in questionable Alzheimer's disease. Ann. Neurol. 56.

Dickerson, B.C., Fenstermacher, E., Salat, D.H., Wolk, D.A., Maguire, R.P., Desikan, R., Pacheco, J., Quinn, B.T., Van der Kouwe, A., Greve, D.N., Blacker, D., Albert, M.S., Killiany, R.J., Fischl, B., 2008. Detection of cortical thickness correlates of cognitive performance: reliability across MRI scan sessions, scanners, and field strengths. Neuroimage 39, 10–18.

Du, A.T., Schuff, N., Amend, D., Laakso, M.P., Hsu, Y.Y., Jagust, W.J., Yaffe, K., Kramer, J.H., Reed, B., Norman, D., Chui, H.C., Weiner, M.W., 2001. Magnetic resonance imaging of the entorhinal cortex and hippocampus in mild cognitive impairment and Alzheimer's disease. J. Neurol. Neurosurg. Psychiatry 71, 441–447.

Duyn, J.H., van Gelderen, P., Li, T.Q., de Zwart, J.A., Koretsky, A.P., Fukunaga, M., 2007. High-field MRI of brain cortical substructure based on signal phase. Proc. Natl. Acad. Sci. U. S. A. 104, 11796–11801.

Feczko, E., Augustinack, J., Fischl, B., Dickerson, B., 2009. An MRI-based method for measuring volume, thickness and surface area of entorhinal, perirhinal, and posterior parahippocampal cortex. Neurobiol. Aging 3, 420–431.

Filimonoff, I., 1947. A Rational Subdivision of the Cerebral Cortex. Chicago.

Fischl, B., Dale, A.M., 2000. Measuring the thickness of the human cerebral cortex from magnetic resonance images. Proc. Natl. Acad. Sci. 97, 11044–11049.

Fischl, B., Sereno, M.I., Dale, A.M., 1999a. Cortical surface-based analysis II: inflation, flattening, a surface-based coordinate system. NeuroImage 9, 195–207.

Fischl, B., Sereno, M.I., Tootell, R.B.H., Dale, A.M., 1999b. High-resolution inter-subject averaging and a coordinate system for the cortical surface. Hum. Brain Mapp. 8, 272–284.

Fischl, B., Liu, A., Dale, A.M., 2001. Automated manifold surgery: constructing geometrically accurate and topologically correct models of the human cerebral cortex. IEEE Trans. Med. Imag. 20, 70–80.

Fischl, B., Salat, D.H., Albert, M., Dieterich, M., Haselgrove, C., Avd, K.o.u.w.e., Killiany, R., Kennedy, D., Klaveness, S., Montillo, A., Makris, N., Rosen, B., Dale, A.M., 2002a. Whole brain segmentation: automated labeling of neuroanatomical structures in the human brain. Neuron 33, 341–355.

Fischl, B., Salat, D.H., Busa, E., Albert, M., Dieterich, M., Haselgrove, C., van der Kouwe, A., Killiany, R., Kennedy, D., Klaveness, S., Montillo, A., Makris, N., Rosen, B., Dale, A.M., 2002b. Whole brain segmentation: automated labeling of neuroanatomical structures in the human brain. Neuron 33, 341–355.

Fischl, B., Salat, D., van der Kouwe, A., Makris, N., Ségonne, F., Quinn, B., Dale, A.M., 2004. Sequence-independent segmentation of magnetic resonance images. Neuroimage I23, S69–S84.

Fischl, B., Rajendran, N., Busa, E., Augustinack, J., Hinds, O., Yeo, B.T.T., Mohlberg, H., Amunts, K., Zilles, K., 2008. Cortical folding patterns and predicting cytoarchitecture. Cereb. Cortex.

Fox, N., Crum, W., Scahill, R., Stevens, J., Janssen, J., Rossor, M., 2001. Imaging of onset and progression of Alzheimer's disease with voxel-compression mapping of serial magnetic resonance images. Lancet 358, 201–205.

Fyhn, M., Molden, S., Witter, M., Moser, E., Moser, M., 2004. Spatial representation in the entorhinal cortex. Science 305, 1258–1264.

Geyer, S., Schleicher, A., Zilles, K., 1997. The somatosensory cortex of human: cytoarchitecture and regional distributions of receptor-binding sites. Neuroimage 6, 27–45.

Geyer, S., Schormann, T., Mohlberg, H., Zilles, K., 2000. Areas 3a, 3b, and 1 of human primary somatosensory cortex. Neuroimage 11, 684–696.

Giannakopoulos, P., Hof, P.R., Michel, J.P., Guimon, J., Bouras, C., 1997. Cerebral cortex pathology in aging and Alzheimer's disease: a quantitative survey of large hospital-based geriatric and psychiatric cohorts. Brain Res. Brain Res. Rev. 25, 217–245.

Gomez-Isla, T., Price, J., McKeel, D.J., Morris, J., Growdon, J., Hyman, B., 1996a. Profound loss of layer II entorhinal cortex neurons occurs in very mild Alzheimer's disease. J. Neurosci. 16, 4491–4500.

Gomez-Isla, T., Price, J.L., McKeel Jr., D.W., Morris, J.C., Growdon, J.H., Hyman, B.T., 1996b. Profound loss of layer II entorhinal cortex neurons occurs in very mild Alzheimer's disease. J. Neurosci. 16, 4491–4500.

Hafting, T., Fyhn, M., Molden, S., Moser, M., Moser, E.I., 2005. Microstructure of a spatial map in the entorhinal cortex. Nature 436, 801–806.

Hargreaves, E., Rao, G., Lee, I., Knierim, J., 2005. Major dissociation between medial and lateral entorhinal input to dorsal hippocampus. Science 308, 1792–1794.

Harrison, P.J., 1999. The neuropathology of schizophrenia. A critical review of the data and their interpretation. Brain 122 (Pt 4), 593–624.

Hinds, O.P., Rajendran, N., Polimeni, J.R., Augustinack, J.C., Wiggins, G., Wald, L.L., Rosas, H.D., Potthast, A., Schwartz, E.L., Fischl, B., 2008. Accurate prediction of V1 location from cortical folds in a surface coordinate system. Neuroimage 39, 1585–1599.

Hyman, B.T., 1997. The neuropathological diagnosis of Alzheimer's disease: clinical–pathological studies. Neurobiol. Aging 18, S27–32.

Hyman, B.T., Gomez-Isla, T., 1997. The natural history of Alzheimer neurofibrillary tangles and amyloid deposits. Neurobiol. Aging 18, 386–387 discussion 389–392.

Hyman, B.T., Van Horsen, G.W., Damasio, A.R., Barnes, C.L., 1984. Alzheimer's disease: cell-specific pathology isolates the hippocampal formation. Science 225, 1168–1170.

Insausti, R., 1993. Comparative anatomy of the entorhinal cortex and hippocampus in mammals. Hippocampus 3 (Spec No), 19–26.

Insausti, R., Tunon, T., Sobreviela, T., Insausti, A.M., Gonzalo, L.M., 1995. The human entorhinal cortex: a cytoarchitectonic analysis. J. Comp. Neurol. 355, 171–198.

Insausti, R., Juottonen, K., Soininen, H., Insausti, A., Partanen, K., Vainio, P., Laakso, M., Pitkänen, A., 1998. MR volumetric analysis of the human entorhinal, perirhinal, and temporopolar cortices. Am. J. Neuroradiol. 19, 659–671.

Jaccard, P., 1912. The distribution of flora in the alpine zone. New Phytol. 11.

Jack, C.R., Petersen, R.C., Xu, Y.C., Waring, S.C., O'Brien, P.C., Tangalos, E.G., Smith, G.E., Ivnik, R.J., Kokmen, E., 1997. Medial temporal atrophy on MRI in normal aging and very mild Alzheimer's disease. Neurology 49, 786–790.

Jack Jr., C.R., Petersen, R.C., Xu, Y., O'Brien, P.C., Smith, G.E., Ivnik, R.J., Tangalos, E.G., Kokmen, E., 1998. Rate of medial temporal lobe atrophy in typical aging and Alzheimer's disease. Neurology 51, 993–999.

Jack Jr., C.R., Petersen, R.C., Xu, Y.C., O'Brien, P.C., Smith, G.E., Ivnik, R.J., Boeve, B.F., Waring, S.C., Tangalos, E.G., Kokmen, E., 1999. Prediction of AD with MRI-based hippocampal volume in mild cognitive impairment. Neurology 52, 1397–1403.

Jack Jr., C.R., Petersen, R.C., Xu, Y., O'Brien, P.C., Smith, G.E., Ivnik, R.J., Boeve, B.F., Tangalos, E.G., Kokmen, E., 2000. Rates of hippocampal atrophy correlate with change in clinical status in aging and AD. Neurology 55, 484–489.

Kalus, P., Slotboom, J., Gallinat, J., Federspiel, A., Gralla, J., Remonda, L., Strik, W.K., Schroth, G., Kiefer, C., 2005. New evidence for involvement of the entorhinal region in schizophrenia: a combined MRI volumetric and DTI study. Neuroimage 24, 1122–1129.

Katzman, R., Terry, R., DeTeresa, R., Brown, T., Davies, P., Fuld, P., Renbing, X., Peck, A., 1988. Clinical, pathological, and neurochemical changes in dementia: a subgroup with preserved mental status and numerous neocortical plaques. Ann. Neurol. 23, 138–144.

Kaye, J., Swihart, T., Howieson, D., Dame, A., Moore, M., Karnos, T., Camicioli, R., Ball, M., Oken, B., Sexton, G., 1997. Volume loss of the hippocampus and temporal lobe in healthy elderly persons destined to develop dementia. Neurology 48, 1297–1304.

Killiany, R.J., Gomez-Isla, T., Moss, M., Kikinis, R., Sandor, T., Jolesz, F., Tanzi, R., Jones, K., Hyman, B.T., Albert, M.S., 2000. Use of structural magnetic resonance imaging to predict who will get Alzheimer's disease [see comments] Ann. Neurol. 47, 430–439.

Killiany, R.J., Hyman, B.T., Gomez-Isla, T., Moss, M.B., Kikinis, R., Jolesz, F., Tanzi, R., Jones, K., Albert, M.S., 2002. MRI measures of entorhinal cortex vs hippocampus in preclinical AD. Neurology 58, 1188–1196.

Krimer, L.S., Hyde, T.M., Herman, M.M., Saunders, R.C., 1997. The entorhinal cortex: an examination of cyto- and myeloarchitectonic organization in humans. Cereb. Cortex 7, 722–731.

Laakso, M.P., 2002. Structural imaging in cognitive impairment and the dementias: an update. Curr. Opin. Neurol. 15, 415–421.

Laakso, M.P., Soininen, H., Partanen, K., Helkala, E.L., Hartikainen, P., Vainio, P., Hallikainen, M., Hanninen, T., Riekkinen Sr, P.J., 1995. Volumes of hippocampus, amygdala and frontal lobes in the MRI-based diagnosis of early Alzheimer's disease: correlation with memory functions. J. Neural. Transm., Parkinson's Dis. Dement. Sect. 9, 73–86.

Laakso, M.P., Hallikainen, M., Hanninen, T., Partanen, K., Soininen, H., 2000. Diagnosis of Alzheimer's disease: MRI of the hippocampus vs delayed recall. Neuropsychologia 38, 579–584.

Malikovic, A., Amunts, K., Scheicher, A., Mohlberg, H., Eickoff, S., Wilms, M., Palomero-Gallagher, N., Armstrong, E., Ziles, K., (2007) Cytoarchitectonic analysis of the human extrastriate cortex in the region of V5/MT+: a probabilistic, stereotaxic map of area hOc5. 17: 562–574.

Mungas, D., Jagust, W.J., Reed, B.R., Kramer, J.H., Weiner, M.W., Schuff, N., Norman, D., Mack, W.J., Willis, L., Chui, H.C., 2001. MRI predictors of cognition in subcortical ischemic vascular disease and Alzheimer's disease. Neurology 57, 2229–2235.

Novak, K., Czech, T., Prayer, D., Dietrich, W., Serles, W., Lehr, S., Baumgartner, C., 2002. Individual variations in the sulcal anatomy of the basal temporal lobe and its relevance for epilepsy surgery: an anatomical study performed using magnetic resonance imaging. J. Neurosurg. 96, 464–473.

Ono, M., Kubick, S., Abernathey, C., 1990. Atlas of the Cerebral Sulci. Georg Thieme Verlag, New York.

Pearlson, G.D., Harris, G.J., Powers, R.E., Barta, P.E., Camargo, E.E., Chase, G.A., Noga, J.T., Tune, L.E., 1992. Quantitative changes in mesial temporal volume, regional cerebral blood flow, and cognition in Alzheimer's disease. Arch. Gen. Psychiatry 49, 402–408.

Pennanen, C., Kivipelto, M., Tuomainen, S., Hartikainen, P., Hanninen, T., Laakso, M.P., Hallikainen, M., Vanhanen, M., Nissinen, A., Helkala, E.L., Vainio, P., Vanninen, R., Partanen, K., Soininen, H., 2004. Hippocampus and entorhinal cortex in mild cognitive impairment and early AD. Neurobiol. Aging 25, 303–310.

Perry, G., Selkoe, D.J., Block, B.R., Stewart, D., Autilio-Gambetti, L., Gambetti, P., 1986. Electron microscopic localization of Alzheimer neurofibrillary tangle components recognized by an antiserum to paired helical filaments. J. Neuropathol. Exp. Neurol. 45, 161–168.

Petersen, R.C., Jack Jr., C.R., Xu, Y.C., Waring, S.C., O'Brien, P.C., Smith, G.E., Ivnik, R.J., Tangalos, E.G., Boeve, B.F., Kokmen, E., 2000. Memory and MRI-based hippocampal volumes in aging and AD. Neurology 54, 581–587.

Prasad, K.M., Patel, A.R., Muddasani, S., Sweeney, J., Keshavan, M.S., 2004. The entorhinal cortex in first-episode psychotic disorders: a structural magnetic resonance imaging study. Am. J. Psychiatry 161, 1612–1619.

Rademacher, J., Morosan, P., Schormann, T., Schleicher, A., Werner, C., Freund, H.J., Zilles, K., 2001. Probabilistic mapping and volume measurement of human primary auditory cortex. NeuroImage 13, 669–683.

Rademacher, J., Burgel, U., Zilles, K., 2002. Stereotaxic localization, intersubject variability, and interhemispheric differences of the human auditory thalamocortical system. Neuroimage 17, 142–160.

Ramon y Cajal, S., 1909. Histologie du Système Nerveux de l'Homme et des Vertébrés. Maloine, Paris.

Rogers, J., Morrison, J.H., 1985. Quantitative morphology and regional and laminar distributions of senile plaques in Alzheimer's disease. J. Neurosci. 5, 2801–2808.

Rosene, D.L., Van Hoesen, G.W., 1987. The hippocampal formation of the primate brain: a review of some comparative aspects of cytoarchitecture and connections. In: Jones, EG, Peters, A (Eds.), Cerebral Cortex. Further Aspects of Cortical Function, Including Hippocampus. Plenum Press, New York, pp. 345–456.

Scahill, R., Schott, J., Stevens, J., Rossor, M., Fox, N., 2002. Mapping the evolution of regional atrophy in Alzheimer's disease: unbiased analysis of fluid-registered serial MRI. Proc. Natl. Acad. Sci. U. S. A. 99, 4703–4707.

Simic, G., Bexheti, S., Kelovic, Z., Kos, M., Grbic, K., Hof, P.R., Kofsovic, I., 2005. Hemispheric asymmetry, modular variability and age-related changes in the human entorhinal cortex. Neuroscience 130.

Soininen, H.S., Partanen, K., Pitkanen, A., Vainio, P., Hanninen, T., Hallikainen, M., Koivisto, K., Riekkinen Sr, P.J., 1994. Volumetric MRI analysis of the amygdala and the hippocampus in subjects with age-associated memory impairment: correlation to visual and verbal memory. Neurology 44, 1660–1668.

Solodkin, A., Van Hoesen, G.W., 1996. Entorhinal cortex modules of the human brain. J. Comp. Neurol. 365, 610–617.

Talairach, J., Szikla, G., Tournoux, P., Prosalentis, A., Bordas-Ferrier, M., Covello, L., Iacob, M., Mempel, E., 1967. Atlas d'Anatomie Stereotaxique du Telencephale. Masson, Paris.

Talairach, J., Tournoux, P., 1988. Co-Planar Stereotaxic Atlas of the Human Brain. Thieme Medical Publishers, New York.

Talamini, L.M., Meeter, M., Elvevag, B., Murre, J.M., Goldberg, T.E., 2005. Reduced parahippocampal connectivity produces schizophrenia-like memory deficits in simulated neural circuits with reduced parahippocampal connectivity. Arch. Gen. Psychiatry 62, 485–493.

Terry, R.D., Katzman, R., 1983. Senile dementia of the Alzheimer type. Ann. Neurol. 14, 497–506.

Turetsky, B.I., Moberg, P.J., Roalf, D.R., Arnold, S.E., Gur, R.E., 2003. Decrements in volume of anterior ventromedial temporal lobe and olfactory dysfunction in schizophrenia. Arch. Gen. Psychiatry 60, 1193–1200.

Van Hoesen, G.W., Pandya, D.N., 1975a. Some connections of the entorhinal (area 28) and perirhinal (area 35) cortices in the rhesus monkey. I. Temporal lobe afferents. Brain Res. 95, 1–24.

Van Hoesen, G.W., Pandya, D.N., 1975b. Some connections of the entorhinal (area 28) and perirhinal (area 35) cortices in the rhesus monkey. III. Efferent connections. Brain Res. 95, 39–59.

Van Hoesen, G.W., Solodkin, A., 1993. Some modular features of temporal cortex in humans as revealed by pathological changes in Alzheimer's disease. Cereb. Cortex 3, 465–475.

Van Hoesen, G.W., Augustinack, J.C., Dierking, J., Redman, S.J., Thangavel, R., 2000. The parahippocampal gyrus in Alzheimer's disease. Clinical and preclinical neuroanatomical correlates. Ann. N.Y Acad. Sci. 911, 254–274.

Xu, Y., Jack Jr., C.R., O'Brien, P.C., Kokmen, E., Smith, G.E., Ivnik, R.J., Boeve, B.F., Tangalos, R.G., Petersen, R.C., 2000. Usefulness of MRI measures of entorhinal cortex versus hippocampus in AD. Neurology 54, 1760–1767.